

Physics-Transfer Learning for Material Strength Screening

Yingjie Zhao¹, Zian Zhang¹, and Zhiping Xu^{*1}

¹Applied Mechanics Laboratory, Department of Engineering Mechanics, Tsinghua University, Beijing 100084, China

*Corresponding author(s): Zhiping Xu (xuzp@tsinghua.edu.cn).

ABSTRACT

The strength of materials, like many problems in the natural sciences, spans multiple length and time scales, and the solution has to balance accuracy and performance. Peierls stress is one of the central concepts in crystal plasticity that measures the strength through the resistance of a dislocation to plastic flow. The determination of Peierls stress involves a multiscale nature depending on both elastic lattice responses and the energy landscape of crystal slips. Material screening by strength via the Peierls stress from first-principles calculations is computationally intractable for the nonlocal characteristics of dislocations, and not included in the state-of-the-art computational material databases. In this work, we propose a physics-transfer framework to learn the physics of crystal plasticity from empirical atomistic simulations and then predict the Peierls stress from chemically accurate density functional theory-based calculations of material parameters. Notably, the strengths of single-crystalline metals can be predicted from a few single-point calculations for the deformed lattice and on the γ surface, allowing efficient, high-throughput screening for material discovery. Uncertainty quantification is carried out to assess the accuracy of models and sources of errors, showing reduced physical and system uncertainties in the predictions by elevating the fidelity of training models. This physics-transfer framework can be generalized to other problems facing the accuracy-performance dilemma, by harnessing the hierarchy of physics in the multiscale models of materials science.

The development of atomistic simulations with first-principles or empirical force fields has led to revolutionary changes in the research of materials sciences¹⁻³. *In silico*, chemically accurate material databases were constructed, allowing high-throughput materials screening and discovery⁴, spanning a wide spectrum of materials from crystals, and molecules, to polymers, where the chemical composition and atomic-level structures are encoded^{1,2,5,6}. However, material properties beyond those of the equilibrium structures such as the strength are rarely reported due to the high computational costs of density functional theory (DFT) and Hartree-Fock (HF) methods, which limits the capability of the discovery of materials with microstructural complexities towards industrial interests⁷⁻¹². Even for single crystals, dislocations can be nucleated under mechanical loads, evolving cooperatively into complex networks, and playing crucial roles in the plasticity of solids. A multiscale framework is needed to address the problem.

To include mesoscale physics in the computational paradigm, the crystal plasticity (CP) theory was developed, where plastic flow and hardening behaviors during material deformation are modeled in a multiscale framework bridging the atomic-scale lattice dynamics and continuum-level stress/strain fields¹³. The plastic strain in crystalline grains is calculated from physical models with dislocation density considered as the state variable, or phenomenological rules for crystalline slips. One of the key material parameters in CP models is the critical resolved shear stress (CRSS), τ_c , which determines the activation of specific slip systems. The kinetic law on a slip system, α , then follows $\dot{\gamma}^\alpha = \dot{\gamma}_0 \left| \frac{\tau^\alpha}{\tau_c} \right|^{1/m} \text{sgn}(\tau^\alpha)$, where $\dot{\gamma}^\alpha$ and τ^α are the shear rate and resolved shear stress, $\dot{\gamma}_0$ and m are material parameters that quantify the reference shear rate and the rate sensitivity of slip, respectively¹³. CRSS can be separated into a thermally dependent term arising from short-range stress fields associated with the thermal activation of dislocations, and an athermal term that is attributed to the presence and interactions with other dislocations¹⁴. In CP models, CRSS is a phenomenological parameter often obtained by fitting experimental results^{15,16}. Alternatively, the Peierls stress (τ_p) defined as the minimum shear stress required to move a single dislocation of unit length in a perfect crystal in the absence of thermal activation (Fig. 1a) is also used in the literature for CRSS¹⁷. The Peierls stress can be obtained from full-atom molecular dynamics (MD) simulations (Fig. 1b). However, the strain inhomogeneity induced by a dislocation usually spans 10 – 20 nm, which cannot be directly calculated from first-principles calculations. Previous studies are thus limited by the use of empirical force fields¹⁸. In practice, the Peierls-Nabarro (PN) model offers a simplified approach to derive the Peierls stress with the assumptions of sinusoidal interfacial restoring stress and a rigidly shifting dislocation, where the structure of a dislocation core is determined by minimizing the elastic energies and lattice misfit¹⁹. The success of the PN model suggests that the Peierls stress is controlled by the elastic responses of the crystals and the energy landscape of interfacial slips²⁰⁻²³.

By assuming the existence of such correspondence, we propose a physics-transfer (PT) framework to predict the Peierls stress for a wide spectrum of metallic alloys (fcc Cu, Ni, Al, Au, Pd, Pt, bcc Fe, Mo, Ta, W, hcp Ti, Mg, Zr, Co) at the first-principles level. The general idea follows from the practices in computational materials science, where although high-fidelity, first-principles methods are preferred for quantitative predictions, low-fidelity models using empirical force fields are still valuable for their capability to tackle problems at much larger length and time scales. The maps between the Peierls stress and characteristic materials parameters are trained from empirical or machine-learning force-field (MLFFs) MD simulations following a supervised learning approach and then applied to DFT-calculated parameters to make predictions at the chemically accurate level. This mapping transfers the physics from low-fidelity but efficient force field models to the first-principles methods, successfully resolving the accuracy-performance dilemma. The approach can be integrated with the computational materials databases for high-throughput screening of high-strength alloys.

The accuracy-performance dilemma

The Peierls stress is determined by balancing the competition between elastic distortion and lattice mismatch created by dislocations. The elastic distortion energy is related to the anisotropic elastic constants of the crystal lattice, while the lattice mismatch energy is associated with the generalized stacking fault energy (GSFE) surface, also known as the γ surface²². The γ surface describes the energy difference between a mismatched lattice and the crystal itself with a specific crystal plane. The energy corrugation characterized by the γ surface is usually constructed by rigidly displacing the two half-crystals at the slip plane along different slip directions. The atoms are relaxed in the direction normal to the slip plane only (see [Methods for details](#))²⁴.

Empirical MD simulations can be used to obtain parameters such as the lattice constants, elastic constants, γ surface, and Peierls stress, but the accuracy is limited by the quality of force fields. We summarize the results calculated using different force fields taken from the interatomic potentials repository^{25,26} (Fig. 1c, Extended Data Fig. 1a, Supplementary Tables 1-3, and Supplementary Figs. 1-8). The predicted energy landscape and Peierls stress display larger dispersion than that of the parameters at the equilibrium states such as lattice and elastic constants (Extended Data Fig. 1b). One of the reasons behind this dispersion is that most force fields are fitted only to the equilibrium structures and lattice cohesion, and are not capable of modeling dislocation slips where the atomic-level configurations deviate significantly from the crystalline structures.

First-principles approaches directly include the effects of electronic structures in predicting material properties and provide chemically accurate models in the condition that the many-body exchange and correlation are well treated²⁷. Density functional theory (DFT) calculations were widely used to calculate the structural and mechanical properties of materials and were shown to be chemically accurate. Comprehensive computational material databases based on DFT calculations were developed, offering a wide spectrum of equilibrium material properties such as the lattice constants, elastic constants, and phase diagrams^{1,2}. However, the direct DFT calculations of the Peierls stress require a relatively large system of several nanometers. For example, a distance of 4 nm is required to study dislocation dissociation in copper, which is not practical for DFT calculations due to their much higher computational costs compared to MD simulations with empirical force fields^{23,28}.

Recent progress in computational hardware and software promotes the development of MLFFs, which harness neural networks to model the potential energy surfaces with the precision of the training set, mostly from first-principles calculations²⁹⁻³¹. MLFFs learn the dependence of the potential energy of a system on the atomic positions. The size effects in direct DFT calculations can be mitigated if this mapping accommodates all atomic environments encountered in the MLFF simulations, and the locality holds well³². The Peierls stress predicted by the MLFFs thus serves as a benchmark to validate the PT predictions. However, the accuracy of the state-of-the-art MLFF predictions for non-equilibrium structures such as those containing dislocations is usually limited compared to the equilibrium features³³, and the MD simulations to predict the Peierls stress using MLFFs still need careful design of the models and simulation parameters to mitigate the effects of sample sizes, loading geometries, and kinetics³⁴. In addition, MLFFs have higher computational costs than common empirical force fields such as EAM and MEAM. A direct mapping between the DFT-derived γ surface and the Peierls stress can thus have the advantage of facilitating fast material screening.

Physics-transfer predictions

To address the accuracy-performance dilemma, we propose a PT framework by assuming that the physics (\mathcal{P}) behind the mapping (\mathcal{M}) transferred across models at different levels of fidelities (\mathcal{F}), such as the atomistic simulations using empirical force fields and DFT calculations, respectively (Fig. 1d). The mapping can be formally written as $\mathcal{M}(\mathcal{P}, \mathbf{x}, \mathcal{F}) \rightarrow \mathcal{O}$, where \mathcal{O} is the objective properties under the accuracy-performance dilemma and \mathbf{x} is the characteristic materials parameters. The physics \mathcal{P} can be learned from low-fidelity (LF) calculations as $\mathcal{M}(\mathcal{P}, \mathbf{x}_{\text{LF}}, \text{MD}) \rightarrow \mathcal{O}_{\text{LF}}$ and then transferred to high-fidelity (HF) calculations to predict the objective properties for higher accuracy, $\mathcal{M}(\mathcal{P}, \mathbf{x}_{\text{HF}}, \text{DFT}) \rightarrow \mathcal{O}_{\text{HF}}$. To apply the PT framework to the predictions of Peierls stress, we first use empirical force fields including EAM and MEAM with different force-field

parameters to calculate the elastic constants, γ surfaces, and Peierls stresses. Digital libraries are constructed for the fcc system (Cu, Ni, Al, Au, Pd, Pt), the bcc system (Fe, Mo, Ta, W), and the hcp system (Ti, Mg, Zr, Co). Feedforward neural networks and pre-trained ResNet are adopted to embed the latent features of the elastic constants and γ surfaces, respectively³⁵ (Fig. 1e). The extracted features of elastic properties and energy corrugation are combined in the latent space and then mapped to the target feature, the Peierls stress. The well-trained machine learning (ML) model is then applied to DFT-calculated elastic constants and γ surfaces of new slip systems, and used to predict their Peierls stresses.

To assess the accuracy of the PT predictions, we first calculate the Peierls stress directly by utilizing different methods of calculations, including EAM, MLFFs, DFT, PT-EAM, and PT-MLFFs for small systems (annotated as ‘S’, containing 244 atoms in a 3.48 nm \times 0.41 nm \times 1.90 nm supercell for the fcc system that suffer from strong size effects in predicting the plasticity of bulk materials. The results in Figs. 2a and 2b indicate that the well-trained neural networks effectively learn the physical mapping between the Peierls stress and the characteristic elastic and surface parameters. The PT-EAM predictions are quantitatively close ($< 48.91\%$) to those from DFT and MLFF calculations. In comparison, those obtained from EAM models show a significant deviation by 221.27% from the DFT predictions (Fig. 2c for Cu $\{111\}\langle 110\rangle$). The time cost of statistical inference in the PT approach is within several milliseconds on an Intel(R) Core(TM) i5-8250U computer with 4 cores), which is significantly lower than that of simulations based on DFT, MLFFs, and EAM (Fig. 2d). These results obtained for small systems successfully demonstrate advantages in the accuracy and efficiency of the PT approach to predict the Peierls stress.

We then consider large models (‘L’, ~ 0.8 million atoms in a 160 nm \times 2 nm \times 40 nm supercell) for 3 crystalline structures (fcc, bcc, hcp) with their associated specific slip systems (Figs. 2e, 2g, and 2i), where direct DFT calculations are not intractable. MD simulations using MLFFs are performed to validate the accuracy of PT predictions from EAM and MEAM models. The results show good consistency (with errors $e = 12.55\%$, 48.09%, 4.30% for Cu $\{111\}\langle \bar{1}10\rangle$, Fe $\{110\}\langle 111\rangle$, Ti $\{10\bar{1}0\}\langle 11\bar{2}0\rangle$ in prediction, respectively) and superior performance compared to the EAM results with $e = 33.07\%$, 72.02%, 13.89% (Figs. 2f, 2h, and 2j). By comparing the results obtained for the small and large systems, we also noted that the size effects are more significant for the empirical force fields. The PT framework thus demonstrates high efficiency compared to DFT and MLFF calculations that can mitigate the size effects, and chemically accurate predictions compared to empirical force fields such as EAM (Supplementary Fig. 9). Table 1 summarizes the Peierls stresses for different slip systems calculated by EAM, PT-EAM, PT-MLFFs, and MLFFs.

Uncertainty quantification

For the Peierls stress predictions, uncertainties exist among different theoretical approaches. Uncertainty quantification (UQ) of these methods is of crucial importance in evaluating and selecting the models. Fig. 2k shows the error maps for various calculation methods. The predictions of small systems with EAM (EAM-S) contain physical uncertainties on the potentials and system uncertainties in size effect. The calculations of small systems with DFT (DFT-S) eliminate physical uncertainties but still suffer from system uncertainties. The predictions of large systems using EAM (EAM-L) with weaker size effects reduce system uncertainties but retain the physical uncertainties. Both PT-EAM predictions and MLFFs calculations eliminate physical and system uncertainties, but PT predictions are superior in computational efficiency, in both the training and inference processes. The uncertainties of different approaches are quantitatively decomposed in Fig. 2l. The uncertainty of prediction using EAM-S contains physical, system errors (99.05% in total) and the inference error (0.95%) by considering the MLFF results as the ground truth. For EAM-L, their contributions are 62.85% and 37.15%, respectively. The PT-EAM prediction only involves uncertainty of inference ($e = 12.55\%$). The low uncertainty of inference compared to the physical and system errors demonstrates the power of the PT framework and can be estimated from the theory of machine learning (Supplementary Section 1, Supplementary Fig. 10)^{36,37}.

The learned physics is limited by the fidelity of digital libraries. Databases constructed with well-trained MLFFs are expected to offer more accurate physics than EAM or MEAM, although their computational costs are high, and a full set of MLFFs for all metal alloys is not available at present. Our studies show that the error of PT-MLFF predictions using the physics learned from MLFF simulations is reduced to $e = 1.51\%$ (Fig. 2l). This few-shot fine-tuning approach utilizing well-trained MLFFs substantially improves the accuracy of the learned physics compared to the database constructed with EAM potentials (Figs. 2c, 2f, 2h, 2j, and 2l).

Discussion

Our PT framework shares some conceptual features with existing ML methods developed to combine multi-fidelity data^{38–40}. Δ -learning predicts high-fidelity properties by learning the discrepancies in predictions from models at different levels of fidelity³⁸. The objective properties are calculated by correcting low-fidelity calculations following a statistical treatment. In a similar spirit, the low-fidelity as a feature (LFAF) method learns the relation between properties obtained from models with different fidelities, and predicts the high-fidelity properties using objective properties and other materials parameters obtained

from low-fidelity models as the input³⁹. Transfer learning pre-trains neural networks on low-fidelity data and fine-tunes the parameters on high-fidelity ones to achieve high accuracy in predictions⁴⁰. However, these methods are statistical in nature and their applications mainly focus on the properties at equilibrium. In supervised learning, it is necessary and beneficial to label data obtained from high-fidelity models in the training process, which are not available for most non-equilibrium properties such as the Peierls stress with chemical accuracy at the DFT level. Our PT framework resolves this constraint from the accuracy-performance dilemma by going beyond the statistical approach and transferring the physics across models with different fidelities, which is characterized by materials parameters that can be obtained from single-point, unit-cell calculations. For example, for the PT predictions of Peierls stresses, the characteristic materials parameters such as the elastic constants and γ surfaces can be corrected by calculations at the level of DFT or DFT-trained MLFFs (Extended Data Figs. 1c, 1d, and Supplementary Fig 11). The Peierls stresses are then predicted accurately and efficiently utilizing the learned physics and chemically accurate materials parameters.

The high accuracy and efficiency of the PT framework allow for single-crystal strength screening and the implementation of mesoscale physics such as the grain texture into the paradigm of high-throughput materials screening and discovery. For a given material genome including the elements and lattice types, the characteristic materials parameters can be estimated by the equilibrium properties reported in the Materials Project (Extended Data Figs. 1e-g). For example, the γ surface can be fitted from a few single-point energy calculations (e.g., intrinsic stacking fault energy γ_{isf} , unstable stacking fault energy γ_{usf} , aligned stacking fault energy γ_{asf} , and the energies of their intermediate configurations) and interpolated using the Fourier series (Extended Data Figs. 1e, 1f and Supplementary Section 2)²⁴. The elastic constants can be determined by the slope of the linear region in stress-strain curves (Extended Data Fig. 1g). The generated characteristic parameters can be used to screen materials by their strengths, a Holy Grail in materials science, through the predicted Peierls stresses, and extension by implementing mesoscale physics models such as crystal plasticity¹³ (Extended Data Fig. 1h).

To address the accuracy-performance dilemma in modeling multiscale problems in computational materials science, we introduced the PT framework. The approach is validated through the Peierls stress predictions, a central parameter in crystal plasticity. Digital libraries including elastic properties, γ surfaces, and Peierls stresses are constructed using atomic simulations, covering various metals with fcc, bcc, and hcp crystal systems obtained from atomistic simulation using empirical potentials. Neural networks are employed to learn the underlying physics. By transferring the physics mappings into the space of the DFT calculations in such a physics-enhanced statistical approach, the Peierls stress can be predicted with simultaneously high efficiency and accuracy. Uncertainty quantification of different computational methods demonstrates that our approach can eliminate the physical uncertainties plagued by low-fidelity models and the system errors caused by the size effects in atomistic simulations. Our PT framework can be integrated with computational material databases and extended to other multiscale problems where both the computational efficiency in modeling large systems and the chemical accuracy to model interatomic interaction are crucial.

Methods

MD simulations

To construct the digital libraries, a wide spectrum of metals with crystalline structures of fcc (Cu, Ni, Al, Au, Pd, Pt), bcc (Fe, Mo, Ta, W), and hcp (Ti, Mg, Zr, Co) is explored. The elastic constants, γ surfaces, and Peierls stresses are calculated using empirical force fields such as EAM and MEAM with parameters reported from different sources^{25,26}, as well as the lattice mismatch energy and slip resistance. The primary slip systems of fcc ($\{111\}\langle\bar{1}10\rangle$) and bcc ($\{110\}\langle 111\rangle$), and the prismatic slip systems of hcp ($\{10\bar{1}0\}\langle 11\bar{2}0\rangle$) are considered.

In calculations of the γ surfaces, a supercell with lattice vectors of \mathbf{a} ($[1\bar{1}0]$), \mathbf{b} ($[11\bar{2}]$), and \mathbf{c} ($[111]$) for the fcc metal is prepared, which contains 64 atoms and 32 atomic layers along the z -axis. A vacuum layer of 30 Å along the z -axis is added to avoid interactions between the periodic images of lattice mismatch. The upper 16 atomic layers are rigidly shifted relative to the lower 16 layers progressively along the z -axis, and independently in the x and y directions, respectively. Relaxation of the atomic layers along the z direction is allowed after the displacement. The γ surfaces are constructed using a 31×31 grid,

$$\gamma(x,y) = \frac{E_m(x,y) - E_0}{S}, \quad (1)$$

where $E_m(x,y)$ is the energies of the lattice with a mismatch at different displacements, $\mathbf{d} = (x,y)$, E_0 is the energy of the crystal in its equilibrium structure, and S is the area of the slip plane.

For the calculations of Peierls stress, a supercell with $\sim 0.8 \times 10^6$ atoms ($160 \text{ nm} \times 2 \text{ nm} \times 40 \text{ nm}$) is prepared. For the fcc metal, lattice mismatch is created between two half-crystals by shifting along the burgers vector by $\mathbf{a}/\sqrt{2}$. Subsequent structural relaxation then creates an initial edge dislocation⁴¹. Molecular statics calculations are used to calculate the Peierls stress identified as the minimum stress at which the motion dislocation is activated⁴². A step-wise strain increment of 10^{-5} is

applied to the supercell. For bcc and hcp metals, similar procedures are adopted but along different lattice orientations and for different slip systems. All MD simulations are performed using the large-scale atomic/molecular massively parallel simulator (LAMMPS)⁴³.

DFT calculations

To validate the hypothesis and feasibility of the PT framework, we directly calculate the Peierls stresses in small systems ('S', with 244 atoms) using Cu as an example. The DFT calculations are carried out using the Vienna *ab initio* simulation package (VASP) using the projector augmented wave (PAW) method and a plane-wave basis^{44,45}. The generalized gradient approximation (GGA) in Perdew-Burke-Ernzerhof (PBE) parametrization is used for the exchange-correlation energy⁴⁶. A supercell for Cu with sizes of 3.48 nm × 0.44 nm × 1.90 nm containing an edge dislocation is prepared by structural relaxation using EAM. A cutoff energy of 500 eV is chosen for the plane waves and a $1 \times 5 \times 1$ ($k_x \times k_y \times k_z$) Monkhorst-Pack **k**-grid is used to sample the Brillouin zone for Cu⁴⁷. The convergence of self-consistent field (SCF) calculations using the plane-wave cutoff and **k**-grid meshing is assured to be below 1 meV/atom (Supplementary Fig. 12). Similar to the setup in MD simulations, a step-wise strain increment of 4×10^{-3} is applied. The Peierls stress is calculated as the minimum stress at which the dislocation is activated to move.

MLFF calculations

The neuroevolution-potential (NEP) framework is adopted to develop MLFFs for fcc Cu, Al, bcc Fe, and hcp Ti⁴⁸. The local atomic environments are encoded by two-body (radial) and three-body (angular) descriptors. A feedforward neural network (FNN) with one hidden layer (30 neurons) is used to predict atomic energies from these descriptors. For systems considering dislocation motion and plastic flow, configurations with applied strain and random perturbation of atomic positions, surface, and stacking fault are included in the training set, and the energies of these configurations are labeled using DFT calculations. Instead of using gradient descent-based back-propagation to update the parameters of neural networks, the separable natural evolution strategy algorithm is implemented in the training process to minimize the relatively complex loss functions⁴⁸. The well-trained MLFFs achieve a prediction accuracy of < 1 meV/atom in the energy of atoms and < 50 meV/Å in the force on atoms. Atomic simulations using the well-trained MLFFs can accurately predict the γ surfaces, which is comparable to the DFT calculations, and process higher computational efficiency (Extended Data Fig. 1c). Details of the MLFFs development will be published elsewhere.

Physics-transfer models

To effectively learn the physical mapping between elastic constants, γ surfaces, and Peierls stresses, we employ a convolutional neural network (CNN) to extract features from the γ surfaces, a FNN to extract the features related to elastic properties and merge them in the latent features space. Then, we use another FNN to predict the Peierls stresses. Considering the small number of samples, which is limited by the number of metal types and potentials, we choose ResNet for the CNN architectures and fine-tune its parameters on ImageNet³⁵. The FNN for extracting elastic properties contains two layers with neuron numbers of 6 (number of elastic features), and 32 (dimension of extracted features), respectively. Following that, the FNN for predicting Peierls stresses has 3 layers with neuron numbers of 64, 32, and 1, respectively. We use the stochastic gradient descent (SGD) optimizer with learning rates of 10^{-3} for dense layers and 10^{-4} for fine-tuning layers⁴⁹. The model is trained and applied to each crystal structure specifically. Training the model from an ensemble of the crystals leads to a compromise in the accuracy, e.g., for certain chemistry (hcp Ti) and others (fcc Cu, bcc Fe) (Supplementary Fig. 13).

Acknowledgments

This work was supported by the National Natural Science Foundation of China through grants 11825203 and 52090032. The computation was performed on the Explorer 1000 cluster system of the Tsinghua National Laboratory for Information Science and Technology.

References

1. Jain, A. *et al.* Commentary: The materials project: A materials genome approach to accelerating materials innovation. *APL Mater.* **1**, 011002 (2013).
2. Saal, J. E., Kirklin, S., Aykol, M., Meredig, B. & Wolverton, C. Materials design and discovery with high-throughput density functional theory: The open quantum materials database (OQMD). *JOM* **65**, 1501–1509 (2013).
3. Fish, J., Wagner, G. J. & Keten, S. Mesoscopic and multiscale modelling in materials. *Nat. Mater.* **20**, 774–786 (2021).
4. Merchant, A. *et al.* Scaling deep learning for materials discovery. *Nature* **624**, 80–85 (2023).
5. Wu, Z. *et al.* MoleculeNet: A benchmark for molecular machine learning. *Chem. Sci.* **9**, 513–530 (2018).
6. Ma, R. & Luo, T. PIIM: A benchmark database for polymer informatics. *J. Chem. Inf. Model.* **60**, 4684–4690 (2020).
7. Mansouri Tehrani, A. *et al.* Machine learning directed search for ultraincompressible, superhard materials. *J. Am. Chem. Soc.* **140**, 9844–9853 (2018).
8. Jin, R., Yuan, X. & Gao, E. Atomic stiffness for bulk modulus prediction and high-throughput screening of ultraincompressible crystals. *Nat. Commun.* **14**, 4258 (2023).
9. Gupta, N., Penev, E. S. & Yakobson, B. I. Polycrystalline morphology and mechanical strength of nanotube fibers. *NPJ Comput. Mater.* **8**, 15 (2022).
10. Liu, F. Y., Ni, B. & Buehler, M. J. Presto: Rapid protein mechanical strength prediction with an end-to-end deep learning model. *Extrem. Mech. Lett.* **55**, 101803 (2022).
11. Yang, L. & Qin, Z. Mycelium-based wood composites for light weight and high strength by experiment and machine learning. *Cell Rep. Phys. Sci.* **4**, 101424 (2023).
12. Lee, S., Zhang, Z. & Gu, G. X. Deep learning accelerated design of mechanically efficient architected materials. *ACS Appl. Mater. Interfaces* **15**, 22543–22552 (2023).
13. Roters, F., Eisenlohr, P., Bieler, T. R. & Raabe, D. *Crystal Plasticity Finite Element Methods* (John Wiley & Sons, 2011).
14. Courtney, T. H. *Mechanical Behavior of Materials* (Waveland Press, 2005).
15. Salem, A., Kalidindi, S. & Semiatin, S. Strain hardening due to deformation twinning in α -titanium: Constitutive relations and crystal-plasticity modeling. *Acta Mater.* **53**, 3495–3502 (2005).
16. Gong, J., Britton, T. B., Cuddihy, M. A., Dunne, F. P. & Wilkinson, A. J. $\langle a \rangle$ Prismatic, $\langle a \rangle$ basal, and $\langle c + a \rangle$ slip strengths of commercially pure Zr by micro-cantilever tests. *Acta Mater.* **96**, 249–257 (2015).
17. Shimanek, J. D., Qin, S., Shang, S., Liu, Z. & Beese, A. M. Predictive crystal plasticity modeling of single crystal nickel based on first-principles calculations. *JOM* **74**, 1423–1434 (2022).
18. Soleymani, M., Parsa, M. & Mirzadeh, H. Molecular dynamics simulation of stress field around edge dislocations in aluminum. *Comput. Mater. Sci.* **84**, 83–96 (2014).
19. Nabarro, F. Dislocations in a simple cubic lattice. *Proc. Phys. Soc.* **59**, 256 (1947).
20. Bulatov, V. V. & Kaxiras, E. Semidiscrete variational Peierls framework for dislocation core properties. *Phys. Rev. Lett.* **78**, 4221 (1997).
21. Nabarro, F. Fifty-year study of the Peierls-Nabarro stress. *Mater. Sci. Eng. A* **234**, 67–76 (1997).
22. Lu, G., Kioussis, N., Bulatov, V. V. & Kaxiras, E. Generalized-stacking-fault energy surface and dislocation properties of aluminum. *Phys. Rev. B* **62**, 3099 (2000).
23. Rodney, D., Ventelon, L., Clouet, E., Pizzagalli, L. & Willaime, F. Ab initio modeling of dislocation core properties in metals and semiconductors. *Acta Mater.* **124**, 633–659 (2017).
24. Su, Y., Xu, S. & Beyerlein, I. J. Density functional theory calculations of generalized stacking fault energy surfaces for eight face-centered cubic transition metals. *J. Appl. Phys.* **126** (2019).
25. Becker, C. A., Tavazza, F., Trautt, Z. T. & de Macedo, R. A. B. Considerations for choosing and using force fields and interatomic potentials in materials science and engineering. *Curr. Opin. Solid State Mater. Sci.* **17**, 277–283 (2013).
26. Hale, L. M., Trautt, Z. T. & Becker, C. A. Evaluating variability with atomistic simulations: The effect of potential and calculation methodology on the modeling of lattice and elastic constants. *Model. Simul. Mat. Sci. Eng.* **26**, 055003 (2018).
27. Martin, R. M. *Electronic Structure: Basic Theory and Practical Methods* (Cambridge university press, 2020).

28. Deng, F., Wu, H., He, R., Yang, P. & Zhong, Z. Large-scale atomistic simulation of dislocation core structure in face-centered cubic metal with deep potential method. *Comput. Mater. Sci.* **218**, 111941 (2023).
29. Ko, T. W. & Ong, S. P. Recent advances and outstanding challenges for machine learning interatomic potentials. *Nat. Comput. Sci.* **3**, 998–1000 (2023).
30. Hedman, D. *et al.* Dynamics of growing carbon nanotube interfaces probed by machine learning-enabled molecular simulations. *arXiv preprint arXiv:2302.09542* (2023).
31. Gong, X., Li, Z., Pattamatta, A., Wen, T. & Srolovitz, D. J. An accurate machine learning interatomic potential for fcc and hcp nickel. *arXiv preprint arXiv:2312.17596* (2023).
32. Zhang, L., Han, J., Wang, H., Car, R. & Weinan, E. Deep potential molecular dynamics: A scalable model with the accuracy of quantum mechanics. *Phys. Rev. Lett.* **120**, 143001 (2018).
33. Takamoto, S. *et al.* Towards universal neural network potential for material discovery applicable to arbitrary combination of 45 elements. *Nat. Commun.* **13**, 2991 (2022).
34. Morrow, J. D., Gardner, J. L. & Deringer, V. L. How to validate machine-learned interatomic potentials. *J. Chem. Phys.* **158** (2023).
35. He, K., Zhang, X., Ren, S. & Sun, J. Deep residual learning for image recognition. In *Proc. IEEE Conf. Comput. Vis. Pattern Recognit. (CVPR)*, 770–778 (2016).
36. Abu-Mostafa, Y. S., Magdon-Ismael, M. & Lin, H.-T. *Learning from Data*, vol. 4 (AMLBook New York, 2012).
37. Feng, Y., Zhang, W. & Tu, Y. Activity-weight duality in feed-forward neural networks reveals two co-determinants for generalization. *Nat. Mach. Intell.* **5**, 908–918 (2023).
38. Ramakrishnan, R., Dral, P. O., Rupp, M. & Von Lilienfeld, O. A. Big data meets quantum chemistry approximations: The Δ -machine learning approach. *J. Chem. Theory Comput.* **11**, 2087–2096 (2015).
39. Batra, R., Pilania, G., Uberuaga, B. P. & Ramprasad, R. Multifidelity information fusion with machine learning: A case study of dopant formation energies in hafnia. *ACS Appl. Mater. Interfaces* **11**, 24906–24918 (2019).
40. Smith, J. S. *et al.* Approaching coupled cluster accuracy with a general-purpose neural network potential through transfer learning. *Nat. Commun.* **10**, 2903 (2019).
41. Bulatov, V. & Cai, W. *Computer Simulations of Dislocations* (Oxford University Press, 2006).
42. Lim, H., Hale, L., Zimmerman, J., Battaile, C. & Weinberger, C. A multi-scale model of dislocation plasticity in α -Fe: Incorporating temperature, strain rate and non-Schmid effects. *Int. J. Plast.* **73**, 100–118 (2015).
43. Plimpton, S. Fast parallel algorithms for short-range molecular dynamics. *J. Comput. Phys.* **117**, 1–19 (1995).
44. Blöchl, P. E. Projector augmented-wave method. *Phys. Rev. B* **50**, 17953 (1994).
45. Kresse, G. & Joubert, D. From ultrasoft pseudopotentials to the projector augmented-wave method. *Phys. Rev. B* **59**, 1758 (1999).
46. Perdew, J. P., Burke, K. & Ernzerhof, M. Generalized gradient approximation made simple. *Phys. Rev. Lett.* **77**, 3865 (1996).
47. Monkhorst, H. J. & Pack, J. D. Special points for Brillouin-zone integrations. *Phys. Rev. B* **13**, 5188 (1976).
48. Fan, Z. *et al.* Neuroevolution machine learning potentials: Combining high accuracy and low cost in atomistic simulations and application to heat transport. *Phys. Rev. B* **104**, 104309 (2021).
49. Hardt, M., Recht, B. & Singer, Y. Train faster, generalize better: Stability of stochastic gradient descent. In *Int. Conf. Mach. Learn. (ICML)*, 1225–1234 (2016).

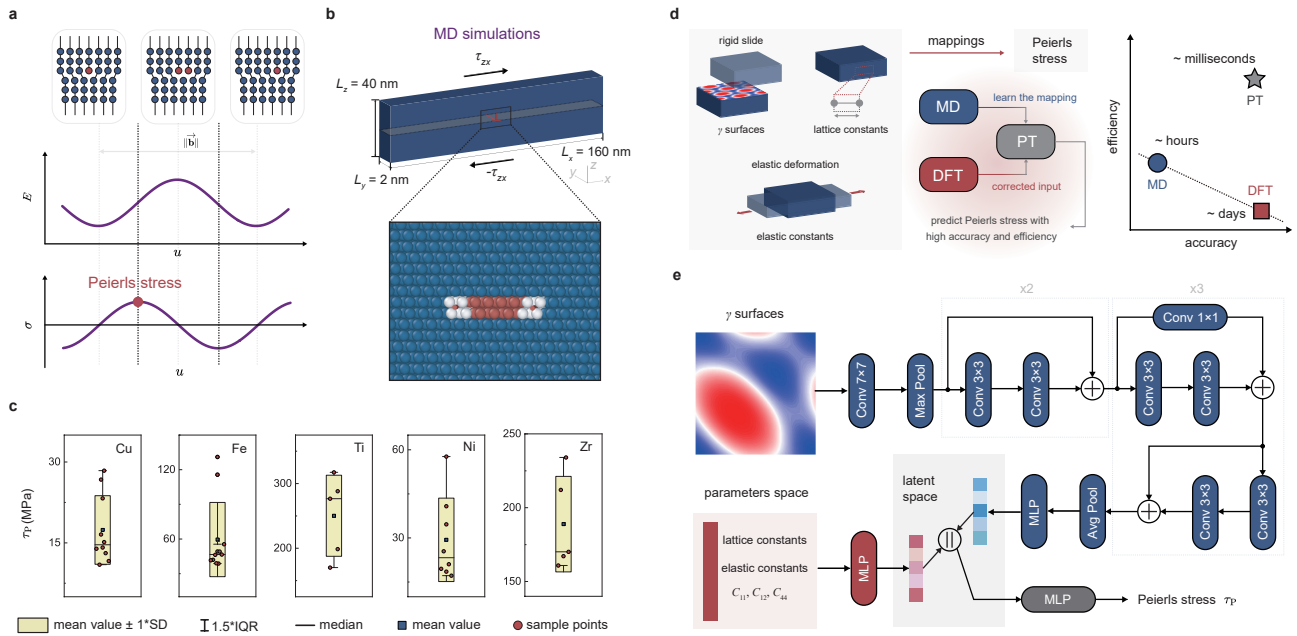


Fig. 1. The physics-transfer framework that resolves the accuracy-performance dilemma in predicting material strength. **a**, Schematic illustration of Peierls stress which determines the slip resistance in plastic deformation. E is the potential energy of configurations with lattice mismatch, σ is the stress on the slip plane, and u is the displacement of mismatch. **b**, Settings of molecular dynamics simulations for Peierls stress (τ_p). **c**, Predictions of Peierls stress using different force fields show strong data dispersion prevalent (Supplementary Tables 1-3). **d**, PT framework transfers the physics from low-fidelity force field models to chemically accurate first-principles methods, effectively addressing the trade-off between accuracy and computational expense. **e**, The architecture of neural networks including the convolutional neural network and multilayer perceptron (MLP) to extract features and map the physics learned from data.

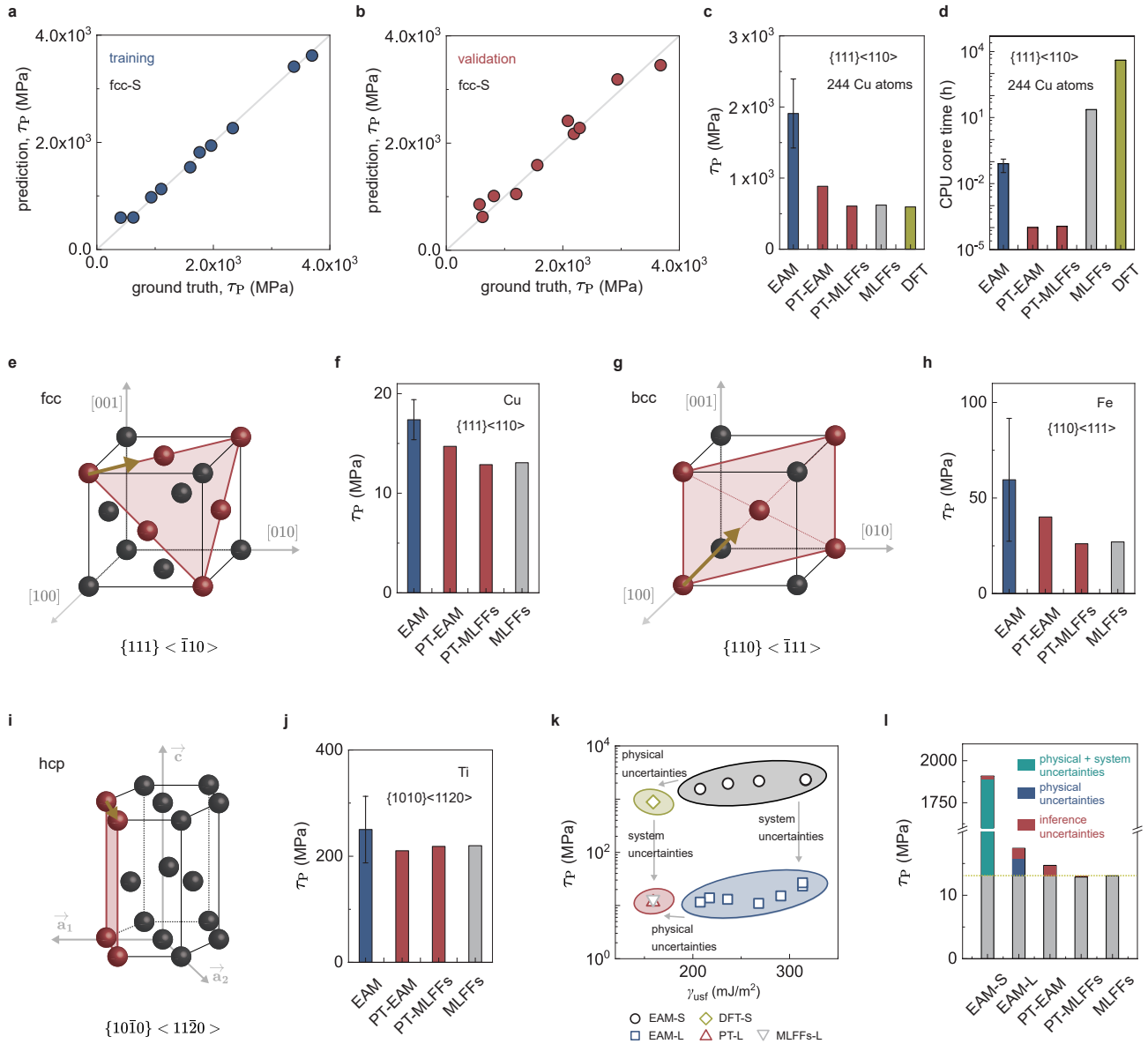
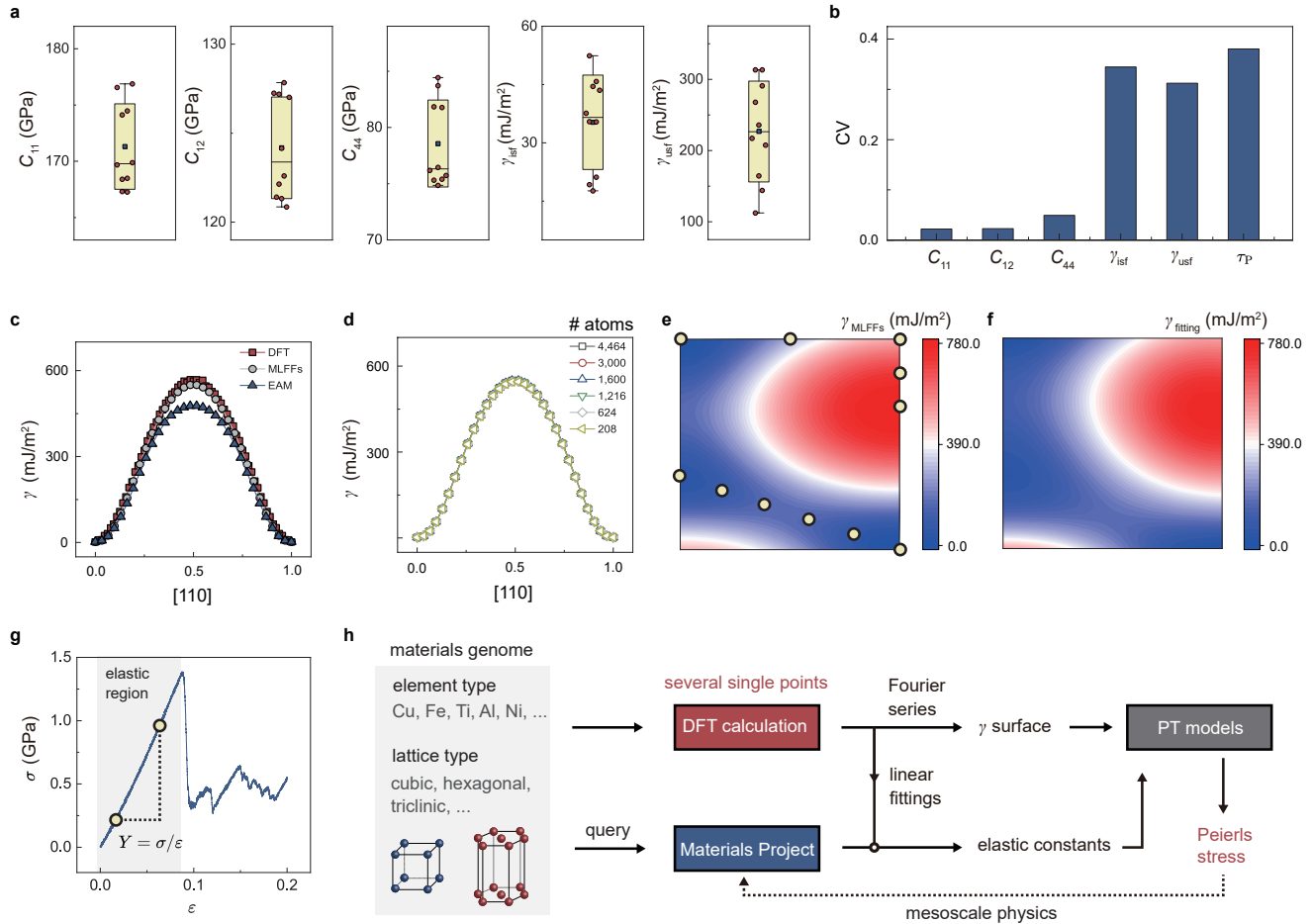


Fig. 2. Predictions of Peierls stress and uncertainties quantification. **a,b**, Well-trained neural networks learn the physical mapping between Peierls stress and characteristic materials parameters obtained from atomistic simulation datasets using empirical force fields (**a**: the training set, **b**: the validation set). ‘S’ denotes the small-supercell model with 244 atoms ($3.48 \text{ nm} \times 0.41 \text{ nm} \times 1.90 \text{ nm}$). **c,d**, PT framework predicts Peierls stress with high accuracy and efficiency. The PT predictions are closely aligned with the outcomes of DFT and MLFF calculations, with a difference below 48.91%, while the results obtained using EAM models deviate substantially from the DFT predictions, with a discrepancy of 221.27% (**c**). The PT approach also reduces the computational time notably by statistical inference, in comparison with atomistic simulations using DFT, MLFFs, or EAM (**d**). **e-j**, PT predictions for different slip systems (**e**: fcc, **g**: bcc, **i**: hcp). The PT predictions show good consistency compared to MLFF simulation results (with errors $e = 12.55\%$, 48.09% , 4.30% for Cu $\{111\}\langle\bar{1}10\rangle$, Fe $\{110\}\langle111\rangle$, Ti $\{10\bar{1}0\}\langle11\bar{2}0\rangle$ in prediction, respectively), and superior accuracy compared to EAM ($e = 33.07\%$, 72.02% , 13.89% (**f,h,j**), respectively). **k**, Uncertainty quantification shows that the PT predictions eliminate physical and system uncertainties. ‘L’ denotes the large-supercell system with $\sim 0.8 \times 10^6$ atoms ($160 \text{ nm} \times 2 \text{ nm} \times 40 \text{ nm}$). **l**, Uncertainty decomposition shows that the inference errors are smaller compared to the physical and system uncertainties. The standard deviation is reported in the error bars.

Table 1. Peierls stress calculated by using EAM, PT-EAM, PT-MLFFs, and MLFFs (the last column is provided for those we developed well-trained MLFFs, [see Methods for details](#)).

Metal	EAM	PT-EAM	PT-MLFFs	MLFFs
Cu $\{111\}\langle\bar{1}10\rangle$	10.96 – 28.40	14.71	12.87	13.07
Fe $\{110\}\langle111\rangle$	38.76 – 131.09	40.09	26.09	27.01
Ti $\{10\bar{1}0\}\langle11\bar{2}0\rangle$	170.08 – 317.36	210.25	218.41	219.70
Al $\{111\}\langle\bar{1}10\rangle$	6.38 – 17.71	11.17	7.22	7.41
Au $\{111\}\langle\bar{1}10\rangle$	4.71 – 11.61	9.45	11.98	-
Ni $\{111\}\langle\bar{1}10\rangle$	17.18 – 57.69	15.26	14.03	-
Pd $\{111\}\langle\bar{1}10\rangle$	14.67 – 14.79	14.28	11.75	-
Pt $\{111\}\langle\bar{1}10\rangle$	14.61 – 35.09	13.86	13.21	-
Mo $\{110\}\langle111\rangle$	50.14 – 95.79	59.38	29.66	-
Ta $\{110\}\langle111\rangle$	23.25 – 23.36	31.45	15.83	-
W $\{110\}\langle111\rangle$	45.01 – 72.98	77.59	38.48	-



Extended Data Fig. 1 Data dispersion, uncertainties, and fitting procedure of characteristic material parameters. a, Dispersion of characteristic materials parameters of Cu obtained from empirical force fields (Supplementary Tables 1). **b**, Coefficient of variation (CV) of material parameters, which is defined as the ratio between the standard deviation σ and the mean μ , that is, $CV = \frac{\sigma}{\mu}$. The predicted γ energy and Peierls stress exhibit a broader range of variation compared to the parameters at equilibrium states, such as elastic constants. **c**, The γ energy curves calculated along the [110] direction using EAM, MLFFs, and DFT. Physical uncertainties of the γ energy that can be eliminated by chemically accurate methods or well-trained MLFFs. **d**, The γ energy curves calculated along the [110] direction using MLFFs with different sizes of simulation supercells. Compared to the physical uncertainties (c), the system errors (d) caused by size effect of γ energy can be ignored. **e**, The γ surface calculated on the {111} plane using MLFFs. **f**, The γ surface fitted by Fourier series on single-point calculations (marked in panel e as scatter points). The fitted energy landscape shows a minor difference with the γ surface obtained with a dense, [31 × 31] grid (see Methods for details). **g**, Stress-strain (σ - ϵ) curves under uniaxial tension along the [100] direction of Cu. The elastic constants (Y) are determined as the slope obtained from single-point calculations. **h**, The scheme to integrate mesoscale physics into the computational material databases with first-principles accuracy.